Supporting Information

Conversion–Lithiophilicity Hosts toward Long-Term and High-Energy-Density Lithium Metal Batteries

Aoming Huang, Hongjiao Huang, Shaoxiong Li, Xiansong Pan, Ai-Yin Wang, Han-Yi Chen, Tao Wang*, Linlin Li, Maxim Maximov, Jianwei Ren, Yuping Wu*, and Shengjie Peng*

Experimental Section

Materials Preparation:

Synthesis of Fe_3C-Fe_2O_3/CNF: All of the analytical reagents were directly used without any further purification. First, 0.6 g of Iron acetylacetonate ($Fe(acac)_3$, Sinopharm) was dissolved in N, N-dimethylformamide (DMF, Sinopharm, 10 ml) under stirring. Second, 1.2 g of polyacrylonitrile (PAN, Macklin, M_w= 150,000) was further added to the above solution with stirring at 60 °C for 12 h to form a precursor solution. Then, the solution was loaded into a 10 ml syringe pump and electrospun at a flow rate of 1 ml h^{-1}. The distance between the needle tip and the aluminum collector was 15 cm, and the operation voltage reached 20 kV. After collection, the as-resultant film was dried overnight in a vacuum oven at 60 °C, and further pre-oxidized at 250 °C for 2 h in air with a ramp of 2 °C min^{-1}, and the obtained product was finally annealed at 800 °C with flowing Ar for 2 h. Accordingly, the black Fe_3C-Fe_2O_3/CNF (EC-LPF) film was prepared.

Synthesis of Fe_2O_3/CNF: Fe_2O_3/CNF (ECF) was prepared by the same procedure as EC-LPF, except that Ar was replaced by H_2/Ar (5/95).

Synthesis of Fe_3C/CNF: Fe_3C/CNF (LPF) was also prepared as the control sample by etching EC-LPF with concentrated HCl.

Characterizations: The morphologies of the samples were investigated by scanning electron microscopy (SEM, Regulus 8100). Transmission electron microscopy (TEM) and high-resolution TEM (HRTEM) images were obtained on FEI Tecnai G2 F20 equipped with energy-dispersive X-ray spectroscopy (EDS, Oxford X-Max). AC-TEM (JEM-ARM200F, JEOL) was employed to investigate the fine structure of the materials at 200 kV. Crystal phases of the samples were identified using X-ray powder diffractometer (XRD, Bruker D8 Advance) with Cu Kα irradiation (λ = 1.54056 Å). Raman spectra were collected on a WITec Alpha 300M+ micro-Raman spectrometer. The surface structure of the nanocomposite was analysed by X-ray

photoelectron spectroscopy (XPS, ESCALAB 250Xi). Thermogravimetry analyses (TGA, Q500) were carried out within a temperature range from 25 to 800 °C under an air flow with a heating rate of 10 °C min^{-1}. To evaluate wettability, the contact angle between self-supporting electrodes and electrolytes was measured using the XG-CAMC33 system (SUNZERN, China) using the sessile drop method.

Electrochemical Measurements: Electrochemical characterization was carried out using 2032-type coin cells. To evaluate the electrochemical deposition behavior and CE, self-supporting EC-LPF, ECF, and LPF were directly used as the working electrodes. The areal mass loading of the EC-LPF electrode is around 1.9 mg cm^{-2}. The lithium metal anode based on ether-based electrolytes could usually provide higher CE than that of carbonate-based electrolytes because of inhibiting of the growth of lithium dendrites. Therefore, 1.0 M lithium bis(trifluoromethanesulfonyl)imide (LiTFSI) in a mixture solution of 1,3-dioxolane and dimethoxyethane (DOL/DME, 1:1 v/v) with 1 wt % lithium nitrate ($LiNO_3$) was used as the main electrolyte. 1.0 M lithium hexafluorophosphate ($LiPF_6$) in a mixture solution of dimethyl carbonate, ethylene carbonate and ethyl methyl carbonate (DMC/EC/EMC, 1:1:1 v/v/v) was selected as the carbonate-based electrolyte. Lithium foil was used as the counter and reference electrode, and Celgard 2400 membrane was selected as the separator. To form a stable SEI on the CNF, the batteries were first cycled between 0 and 1.0 V (versus Li/Li^+) at 0.2 A g^{-1} for three cycles. Then, a fixed amount (1.0 mAh cm^{-2}) of Li metal was plated onto the CNF and then stripped away until 1.0 V at 1.0 mA cm^{-2}. The cycling performance was performed on a NEWARE battery testing system. Then, 3 mAh cm^{-2} of Li was plated onto the EC-LPF, ECF, or LPF at a current density of 1 mA cm^{-2} to form Li/EC-LPF, Li/ECF, and Li/LPF. Symmetric cells were assembled using Li/EC-LPF, Li/ECF, and Li/LPF electrodes to measure the long-term electrochemical behavior of Li plating/stripping. Cyclic voltammetry (CV) was performed on symmetric cells to measure the exchange current density. A fixed sweep rate of 1.0 mV s^{-1} was employed the voltage range from −200 mV to 200 mV. For the full cells, the cathode contains 95 wt % of commercial $LiFePO_4$ powder, 2 wt % of Super-P, and 3 wt % of polyvinylidene difluoride (PVDF) binder using N-methyl-2-pyrrolidone (NMP) as the solvent, and the well-mixed slurry was cast onto carbon-coated Al foil. This ratio is 90:5:5 for $LiNi_{0.8}Co_{0.1}Mn_{0.1}O_2$ (NCM811). The areal capacity loading of $LiFePO_4$ (1C=170 mAh g^{-1}) and NCM811 (1C=200 mAh g^{-1}) cathodes was controlled at about 1.0 mAh cm^{-2}. The capacity ratio of cathode and anode was about 1:2. For full cell testing, unless otherwise specified, a self-supporting electrode loaded with 2 mAh cm^{-2} lithium is utilised. All the cells were

assembled in a glove box with H_2O/O_2 content lower than 0.1 ppm and were tested at room temperature.

For three-electrode cells test, a button type three electrode cell is constructed using a home-made lithium reference electrode. To prepare a lithium reference electrode, wrap one end of the copper wire with lithium foil and then wrap the middle portion of the copper wire with PET tape to prevent short circuits between electrodes. When assembling the cell, two separators are placed to separate the reference electrode from the positive and negative electrodes. The structure of the lithium reference electrode and its positioning within the cell are shown in Figure S17.

For pouch cell, Commercial $LiFePO_4$ cathode single-sided electrode (Shenzhen Kejing Star Technology Co.) was employed to build the Li metal pouch cell. The positive electrode had an areal mass loading of about 14 mg cm^{-2}, with a dimension of 4*5 cm^2. The self-supporting electrode was pre-electroplated with 9.5 mAh cm^{-2} lithium in an electrolytic cell to achieve an N/P ratio of 2. The pouch cell was assembled by a pre-lithiated anode and two slices $LiFePO_4$ cathode electrodes. The same ether-baesd electrolyte and separator as the case for coin full cells were used. Meantime, the pouch cell was filled with ~2 g Ah^{-1} of electrolyte. The formation of the battery is achieved through a single cycle at a current of 10 mA within a voltage range of 2.0 to 4.0 V. The cycle test employs a constant current−constant voltage (CC−CV) protocol, which involves initially charging the battery to 4.0 V at a current rate of 20 mA, maintaining this voltage until the current rate decreases to 5 mA, and subsequently discharging the battery to 2.0 V at a current rate of 20 mA.

Computational methods: We have employed the Vienna Ab-initio Simulation Package (VASP)[1,2] to perform all the density functional theory (DFT) calculations within the generalized gradient approximation (GGA) using the PBE[3] formulation. We have chosen the projected augmented wave (PAW) potentials[4,5] to describe the ionic cores and take valence electrons into account using a plane wave basis set with a kinetic energy cutoff of 400 eV. Partial occupancies of the Kohn−Sham orbitals were allowed using the Gaussian smearing method and a width of 0.05 eV. The electronic energy was considered self-consistent when the energy change was smaller than 10^{-5} eV. A geometry optimization was considered convergent when the force change was smaller than 0.02 eV/Å. Grimme's DFT-D3 methodology[6] was used to describe the dispersion interactions. The adsorption energy (E_b) of adsorbate A was defined as

$$E_b = E_{A/surf} - E_{surf} - E_{A(g)}$$

where $E_{A/surf}$, E_{surf} and $E_{A(g)}$ are the energy of adsorbate A adsorbed on the surface, the energy of clean surface, and the energy of isolated A molecule in a cubic periodic box with a side length of 20 Å and a 1×1×1 Monkhorst-Pack k-point grid for Brillouin zone sampling, respectively.

Finally, transition states for elementary reaction steps were determined by the nudged elastic band (NEB) method. In the NEB method, the path between the reactant and product is discretized into a series of structural images.

Calculate the content by TG

As the ultimate decomposition product of both Fe_3C and Fe_2O_3 is Fe_2O_3, thermogravimetric analysis (TG) cannot directly quantify the respective components in EC-LPF. To address this, an innovative approach was devised, involving the utilization of hydrochloric acid etching to selectively remove Fe_2O_3 while preserving Fe_3C, which is Fe_3C on carbon nanofiber (LPF). Subsequently, by integrating the TG results from two distinct samples—one being the LPF sample where Fe_2O_3 has been etched away, and the other being the original EC-LPF sample—Fe_3C content in the LPF can be calculated. This, in turn, can infer the individual contents of Fe_2O_3 and Fe_3C in the EC-LPF composite material. The calculations could be based on the following equation:

$$\mathrm{Fe_3C\ (I, wt\%)} = \frac{2}{3} \times \frac{\text{Molecular weight of } \mathrm{Fe_3C}}{\text{Molecular weight of } \mathrm{Fe_2O_3}} \times \text{Final weight (I, wt\%)} \quad (1)$$

$$\mathrm{Fe_3C\ (II, wt\%)} = \mathrm{Fe_3C\ (I, wt\%)} / (1 + \mathrm{Fe_2O_3\ (II, wt\%)}) \quad (2)$$

$$\text{Final weight (II, wt\%)} - \mathrm{Fe_2O_3\ (II, wt\%)} = \mathrm{Fe_3C\ (II, wt\%)} \times \frac{3}{2} \times \frac{\text{Molecular weight of } \mathrm{Fe_2O_3}}{\text{Molecular weight of } \mathrm{Fe_3C}} \quad (3)$$

where I and II represent the TG data obtained from the LPF and EC-LPF samples, respectively.

Tafel curve

When the concentration polarization is negligible, the exchange current density can be calculated based on Tafel equation:[7]

$$\eta = \mathrm{a} + \mathrm{b} \log j \quad (1)$$

where j is the current density, η is the overpotential, a and b are constants.

Lithium diffusion coefficient from CV

Lithium diffusion coefficient (D_{Li^+}) was calculate by a series of CV curves at different scan rates based on Randles-Sevcik equation:[8]

$$i_p = 2.69 \times 10^5 n^{3/2} A D_{Li^+}^{1/2} v^{1/2} C \quad (2)$$

where i_p is the peak current (A), A is the area of electrode (1.13 cm^2), n is the number of reaction electrons (n = 1 for Li||$LiFePO_4$ cell), C is the concentration of Li^+ ($C = 2.27 \times 10^{-2}$ mol cm^{-3}), v is the scanning rate (V s^{-1}), and D_{Li^+} is the lithium diffusion coefficient.

Lithium diffusion coefficient from GITT

By the galvanostatic intermittent titration technique (GITT) technique, the Li-ion chemical diffusion coefficients (D_{Li^+}) can be quantitatively determined through the simplified Fick's second law:[9]

$$D = \frac{4}{\pi\tau}\left(\frac{m_B V_m}{M_B S}\right)^2 \left(\frac{\Delta E_S}{\Delta E_t}\right)^2 \quad (3)$$

where τ is the current pulse time (s), V_m, M_B, and m_B are the molar volume, the molecular weight, and the mass of the active material, respectively. S is the geometric area of the electrode. ΔE_S and ΔE_t are the voltage changes during the time period s and after open-circuit stand.

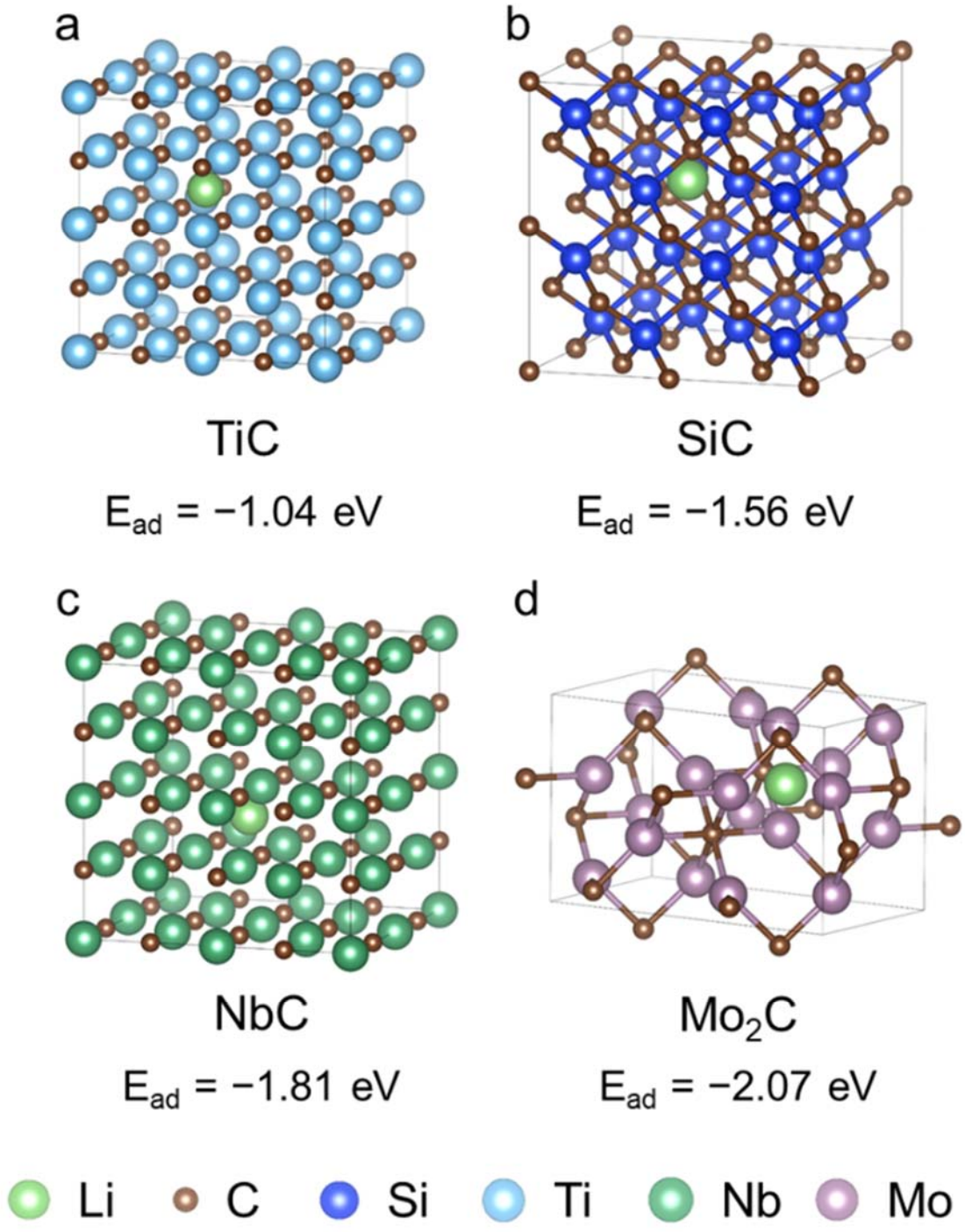

Figure S1. The adsorption structure and the corresponding adsorption energy of Li in (a) TiC, (b) SiC, (c) NbC, and (d) Mo_2C.

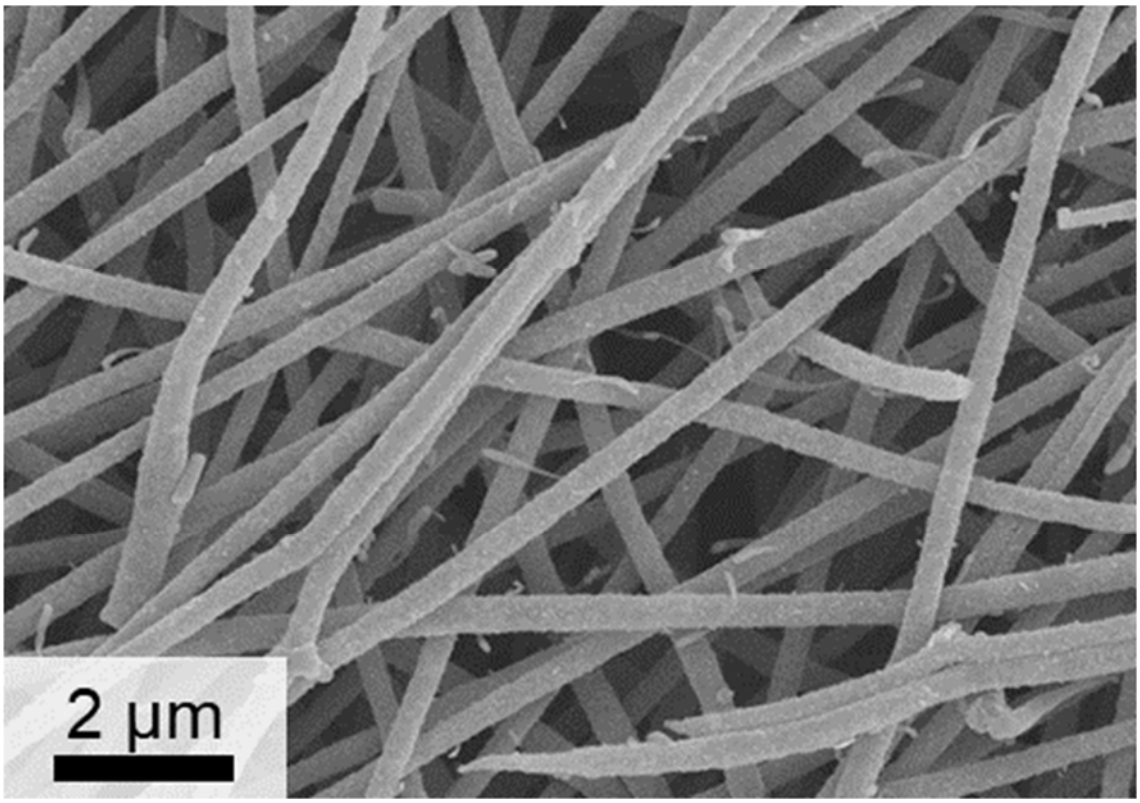

Figure S2. SEM image of EC-LPF.

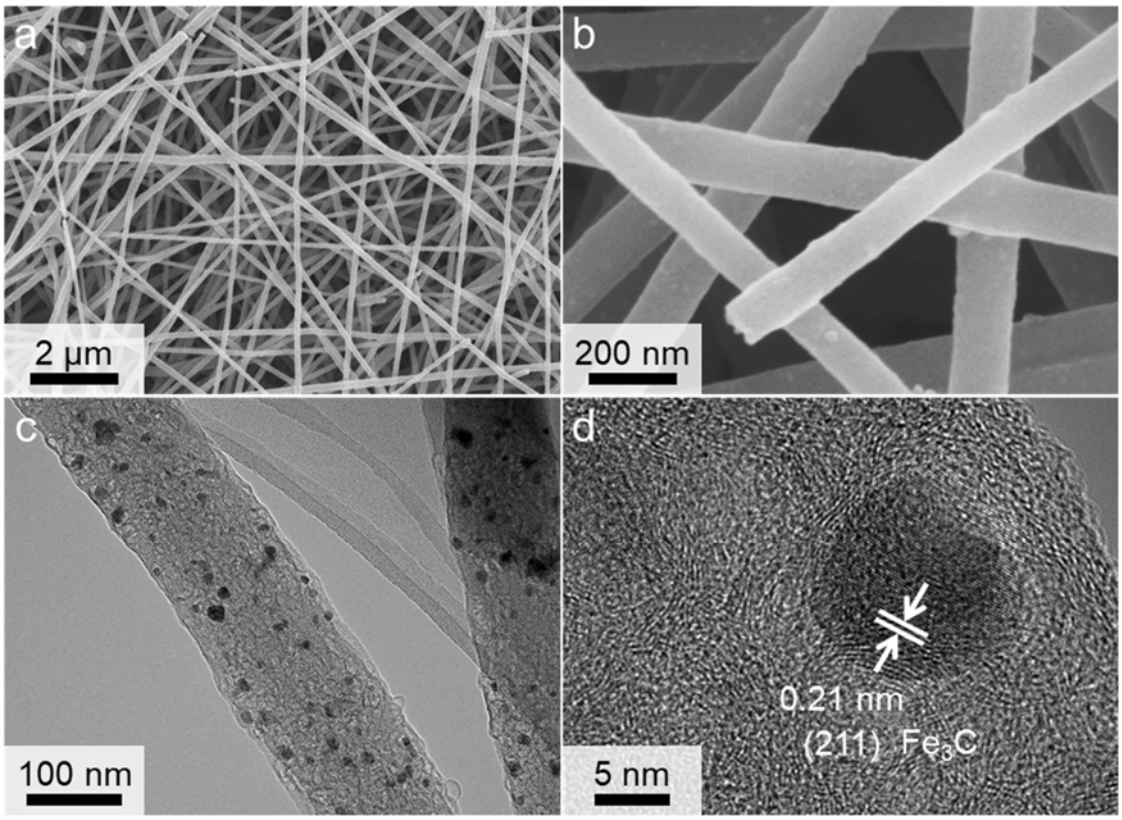

Figure S3. (a-b) SEM and (c-d) TEM images of LPF.

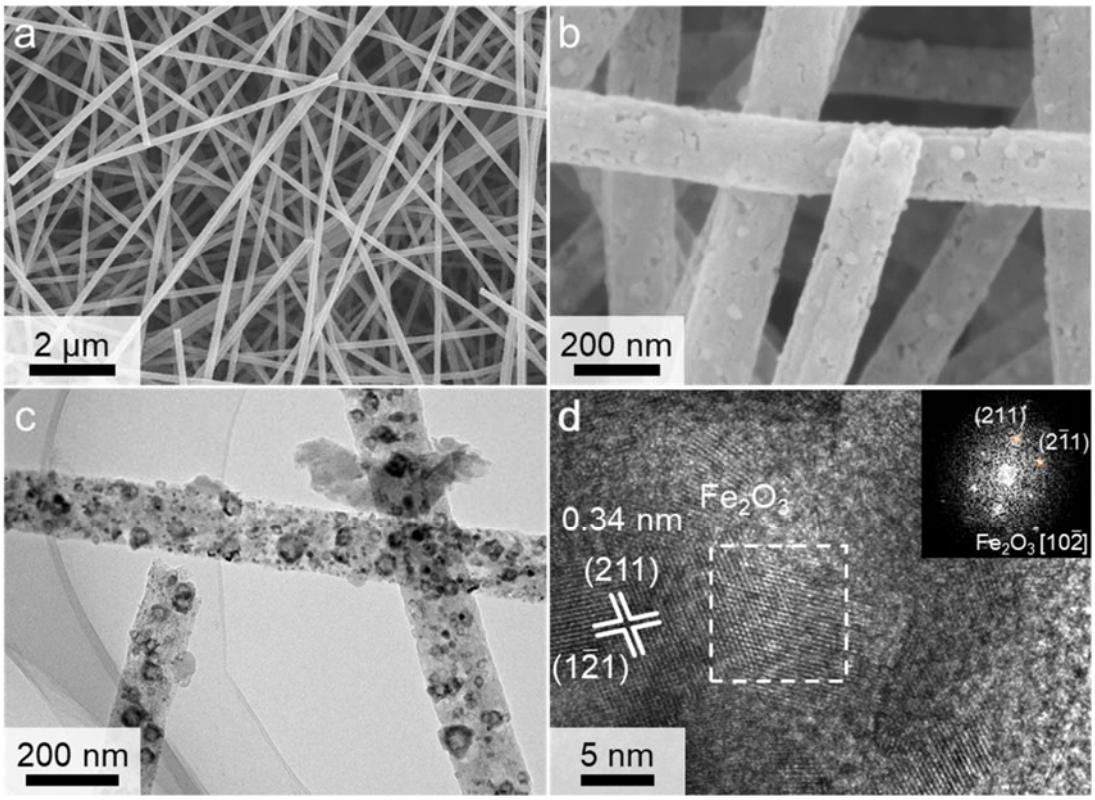

Figure S4. (a-b) SEM and (c-d) TEM images of ECF, inset: corresponding FFT pattern of the squared region highlighted in (d).

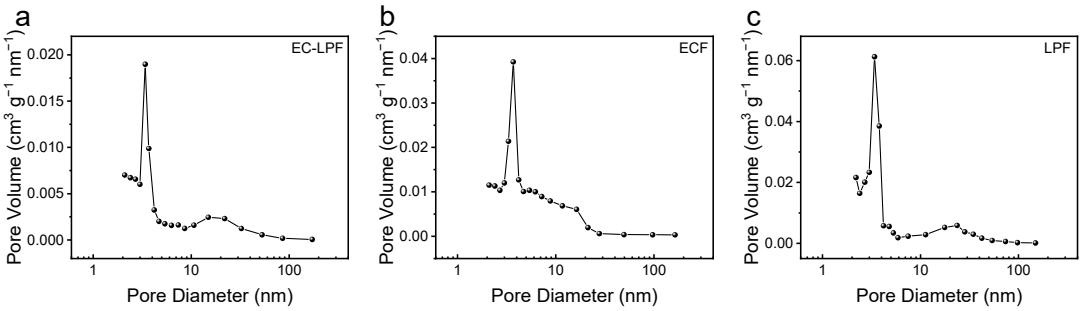

Figure S5. Pore-size distributions of (a) EC-LPF, (b) ECF and (c) LPF.

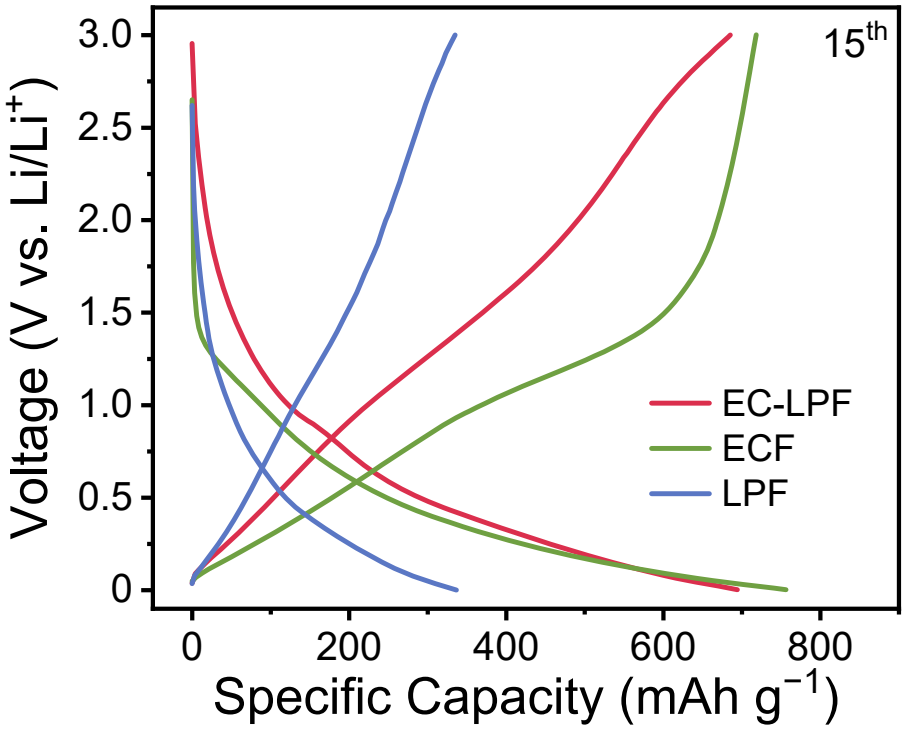

Figure S6. The charge-discharge curve of the self-supporting electrode after 15 cycles.

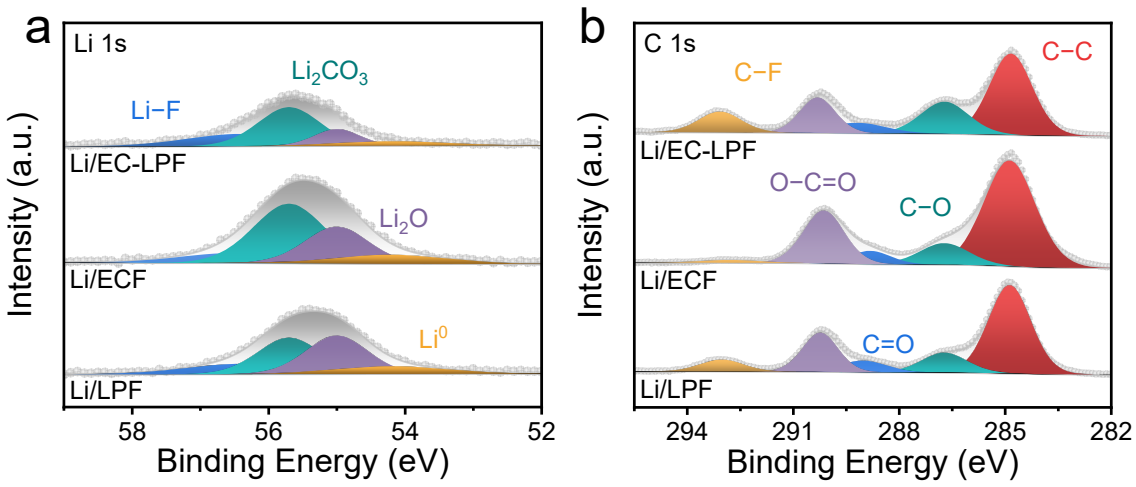

Figure S7. High-resolution XPS spectra of (a) Li 1s and (b) C 1s for self-supporting electrodes after lithium activation.

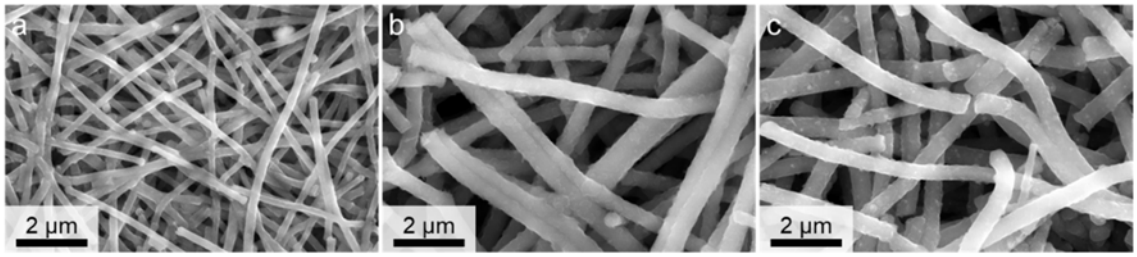

Figure S8. SEM images of (a) EC-LPF, (b) ECF and (c) LPF after lithium activation.

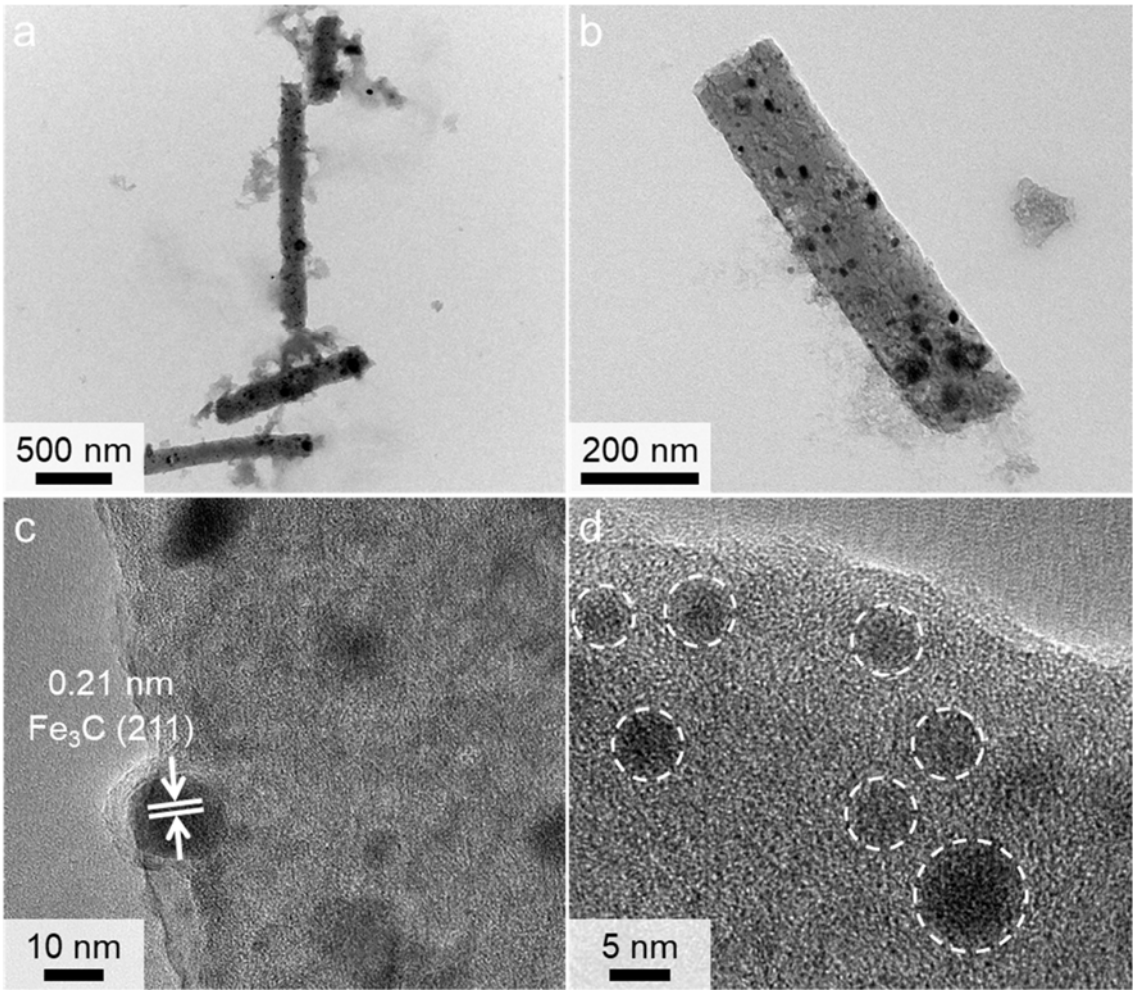

Figure S9. (a-d)TEM images of EC-LPF electrode after multiple cycles of lithium deposition and stripping.

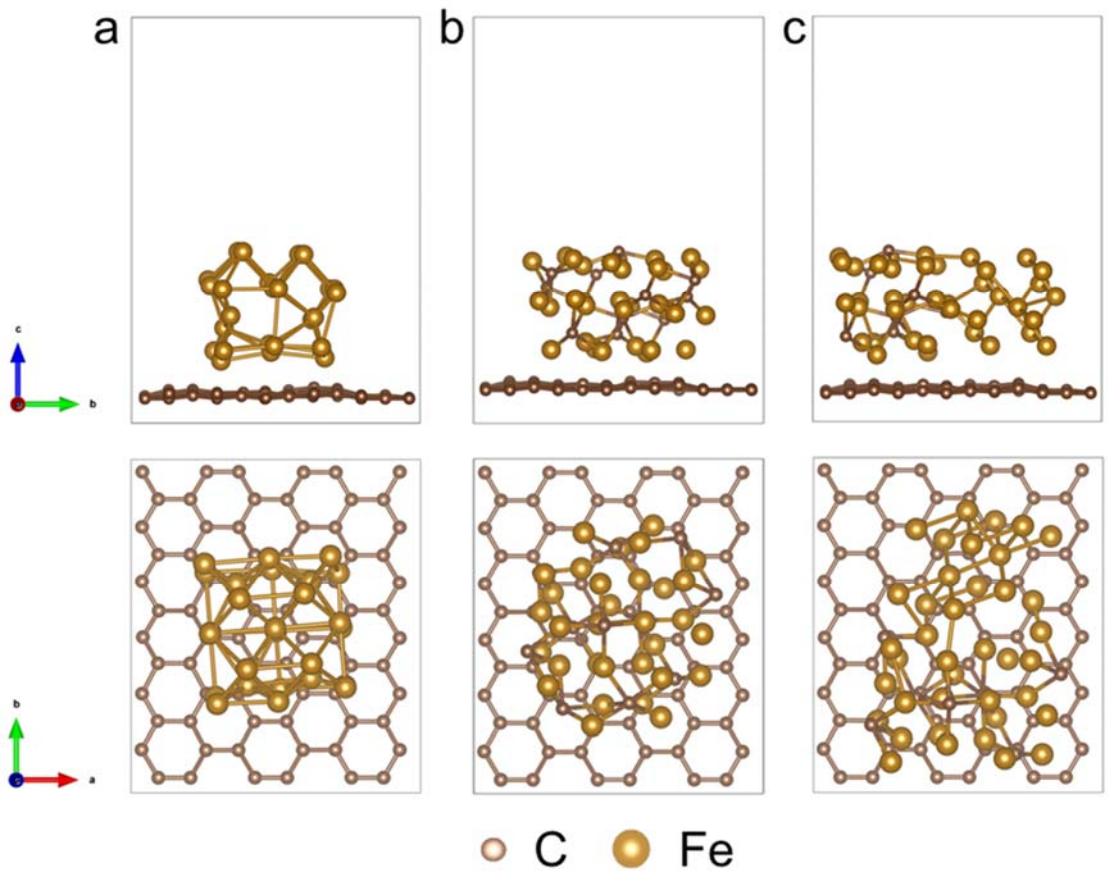

Figure S10. Predicted optimized configurations of (a) Fe/C, (b) Fe_3C/C, and (c) Fe_3C/Fe/C.

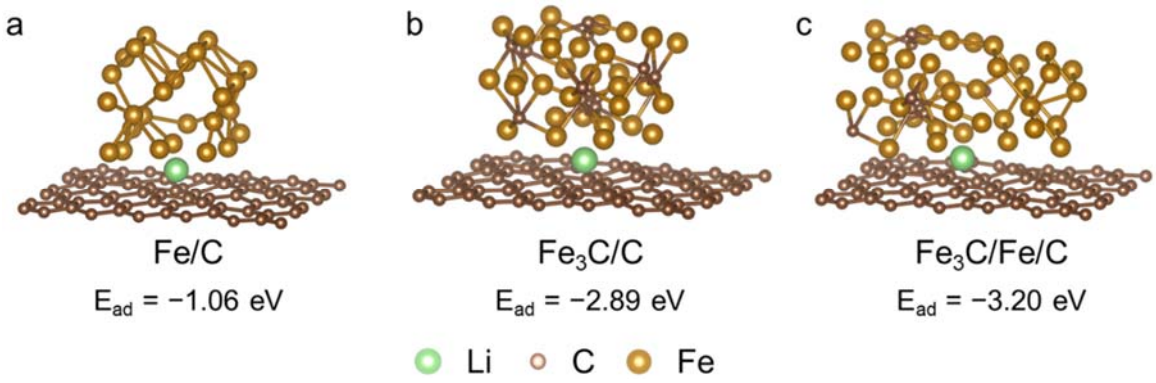

Figure S11. The adsorption structure of Li on interface sites of (a) Fe/C, (b) Fe_3C/C, and (c) Fe_3C/Fe/C.

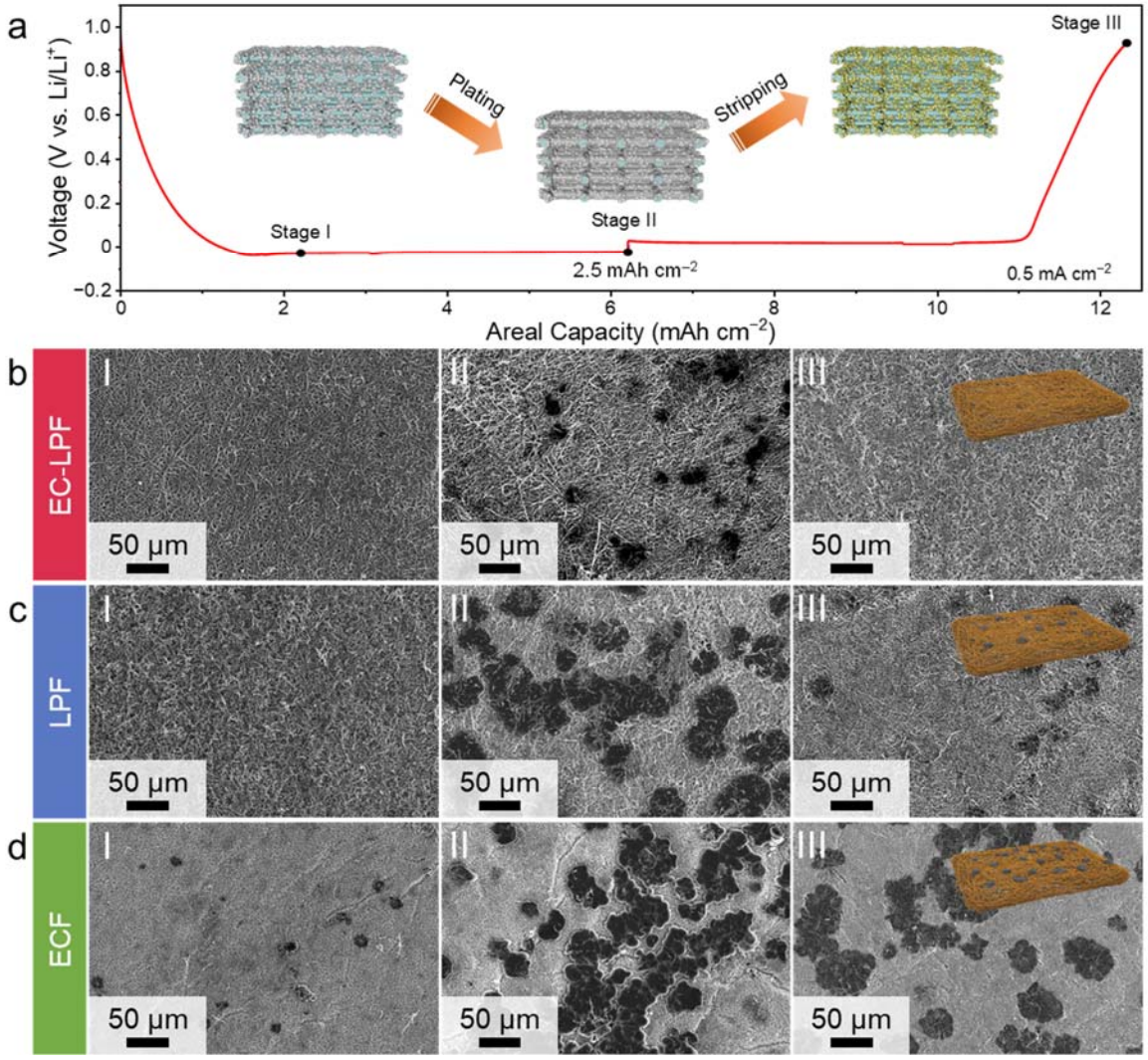

Figure S12. (a) Electrochemical Li plating curve of the EC-LPF electrode at 0.5 mA cm^{-2}. SEM images of (b) EC-LPF, (c) LPF and (d) ECF electrodes after lithium metal plating and stripping.

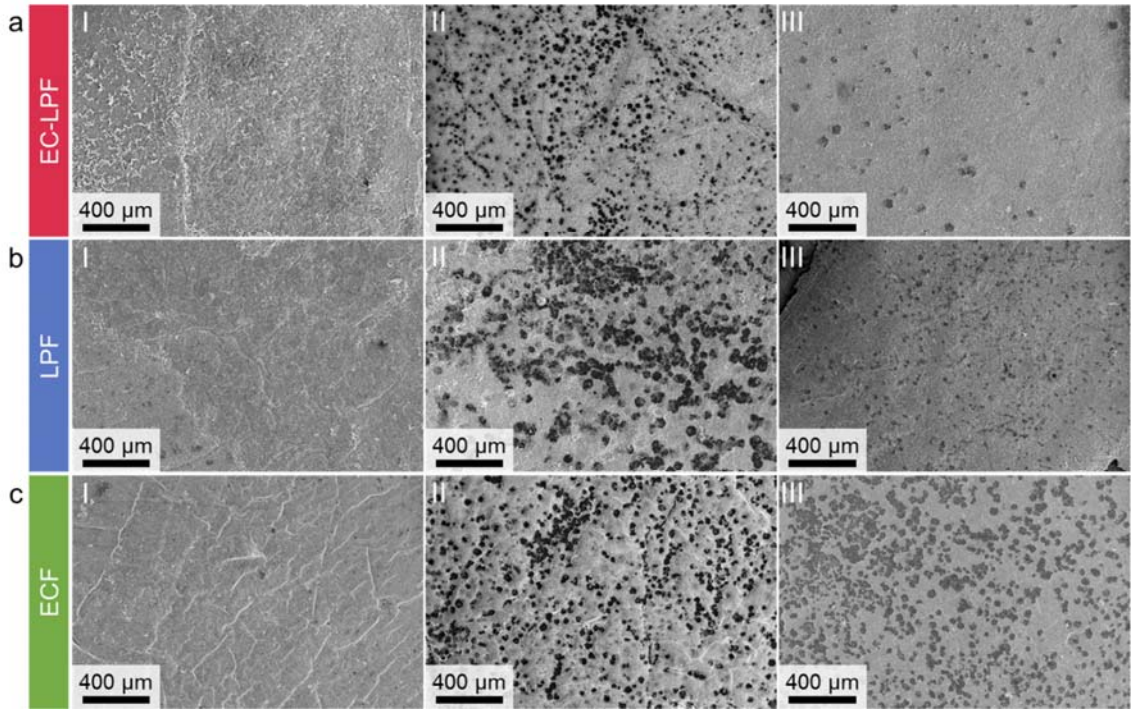

Figure S13. Low magnification SEM images of (a) EC-LPF, (b) LPF and (c) ECF electrodes after lithium metal plating and stripping.

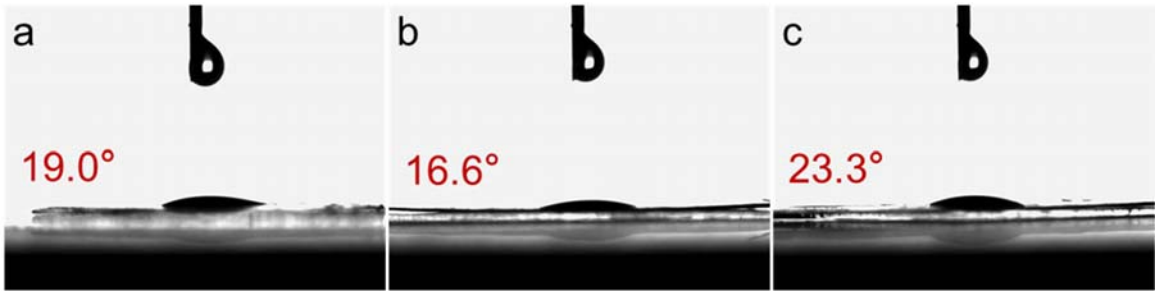

Figure S14. The contact angle tests of (a) EC-LPF, (b) ECF and (c) LPF.

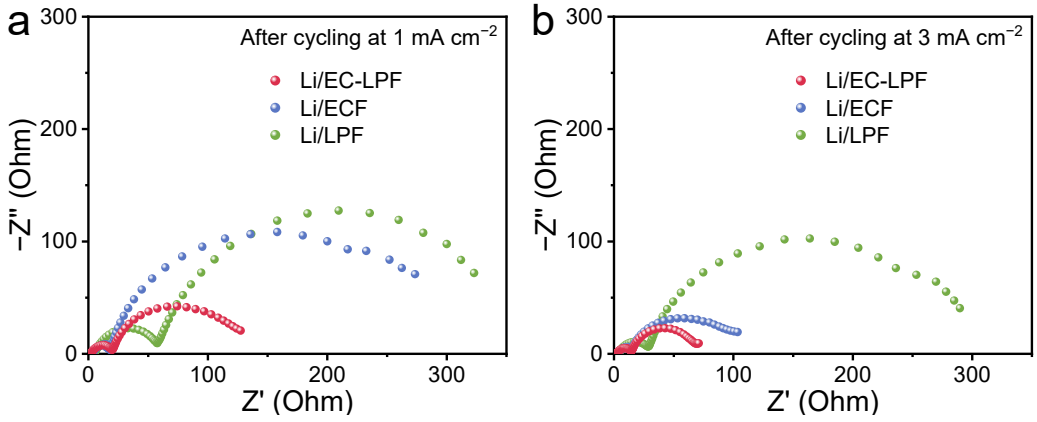

Figure S15. Nyquist plots of symmetric cells after cycles at (a) 1 mA cm^{-2} and (b) 3 mA cm^{-2}.

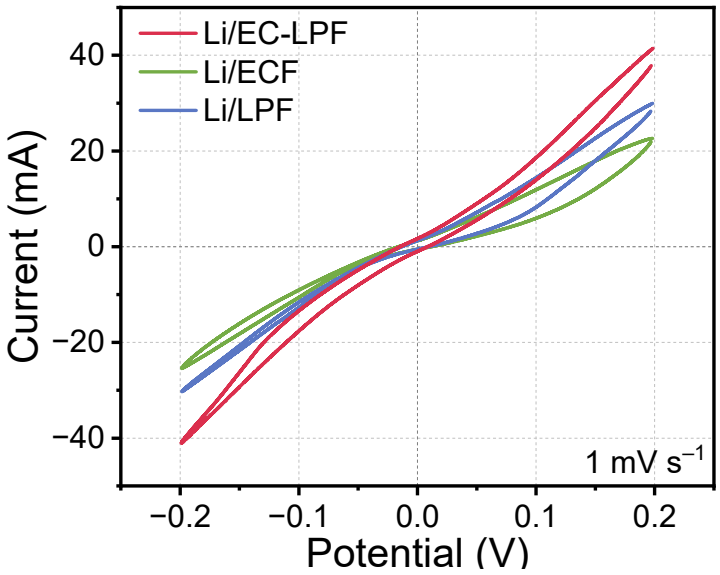

Figure S16. Cyclic voltammetry curve of symmetric cells with a scan rate of 1.0 mV s^{-1}.

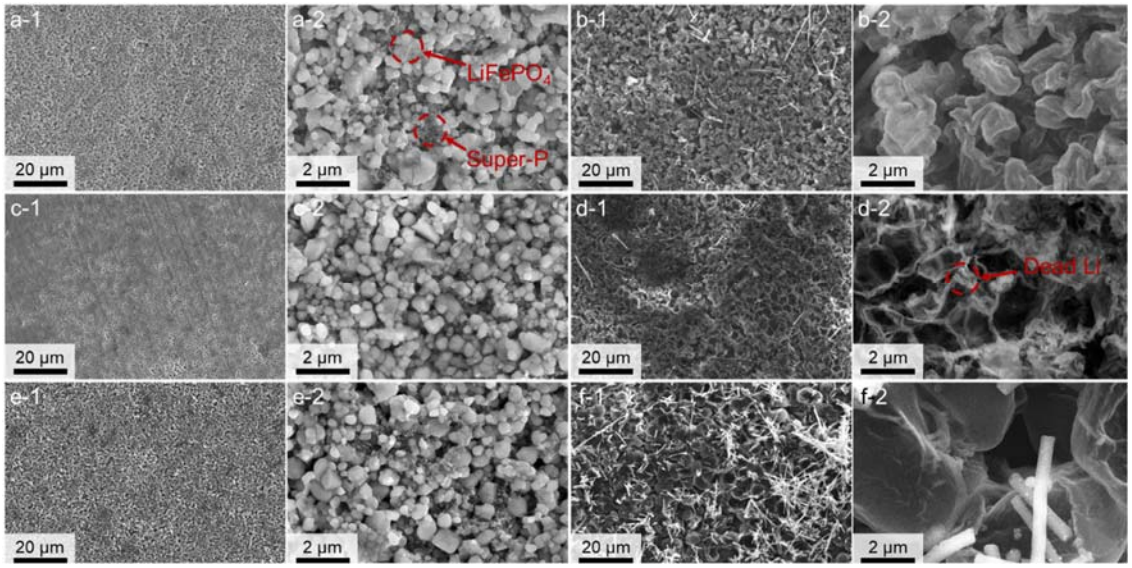

Figure S17. SEM images of a,c,e) cathode and b,d,f) anode after cycling, from a,b) $LiFePO_4$||Li/EC-LPF, c,d) $LiFePO_4$||Li/LPF, and e,f) $LiFePO_4$||Li/ECF full cells, respectively.

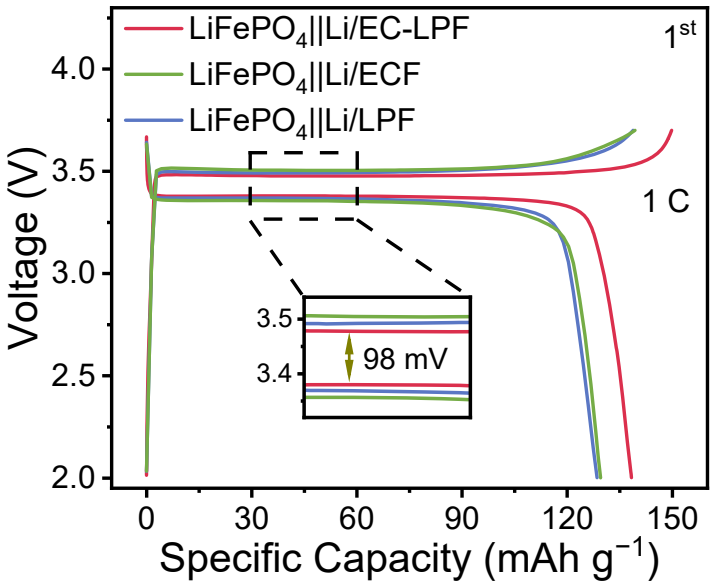

Figure S18. The voltage profiles of the first cycle of $LiFePO_4$ full batteries with different anodes at 1C.

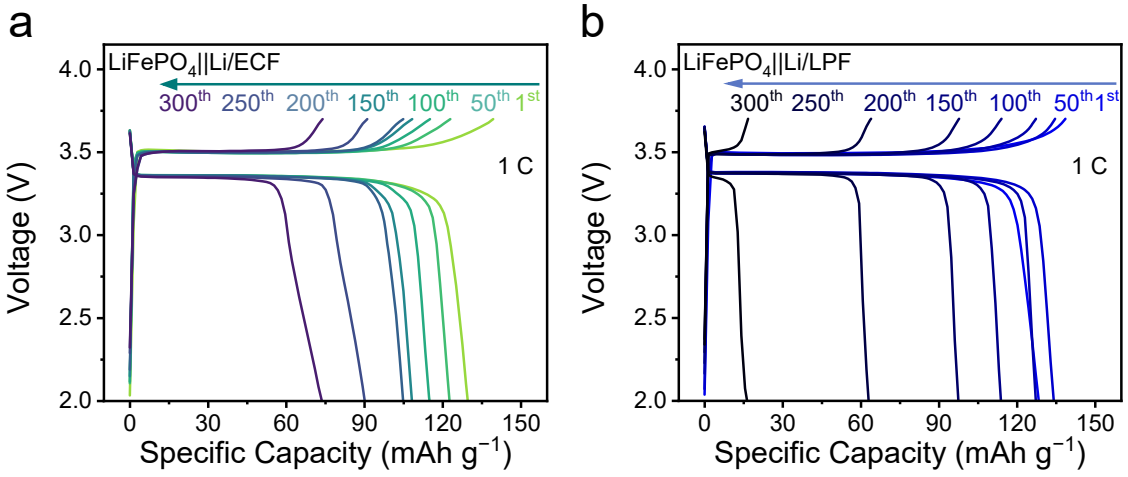

Figure S19. The galvanostatic charge/discharge voltage curves of (a) $LiFePO_4$||Li/ECF and (b) $LiFePO_4$||Li/LPF at different cycle number.

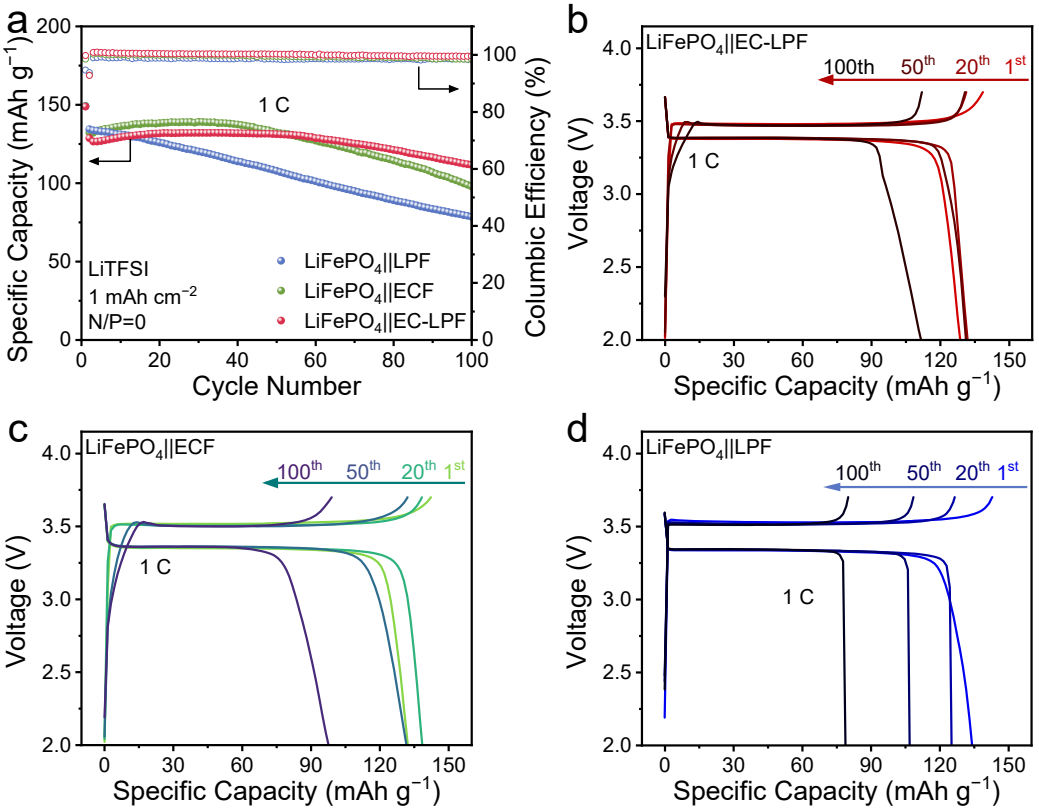

Figure S20. (a) The cycling performance of $LiFePO_4$ full batteries with different Li-free self-supporting anodes at 1C and (b-d) corresponding voltage profiles.

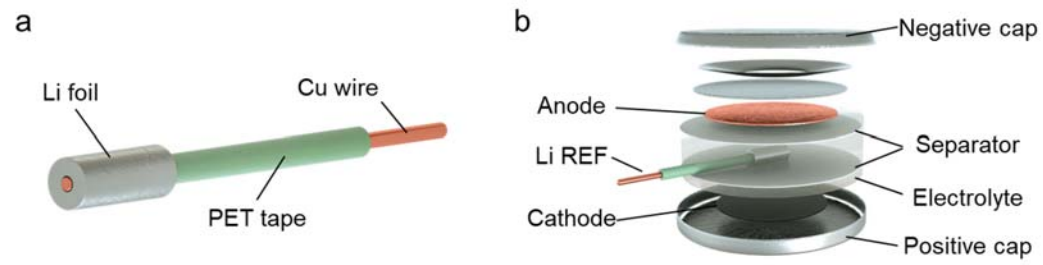

Figure S21. Schematics of the Li reference electrode and a three-electrode coin cell. (a) The Li reference electrode was fabricated by attaching a small piece of Li foil at the tip of a copper wire. (b) The three-electrode coin cell consists of a $LiFePO_4$ cathode, a Li reference electrode sandwiched between two separators, and a self-supporting electrospun fiber anode.

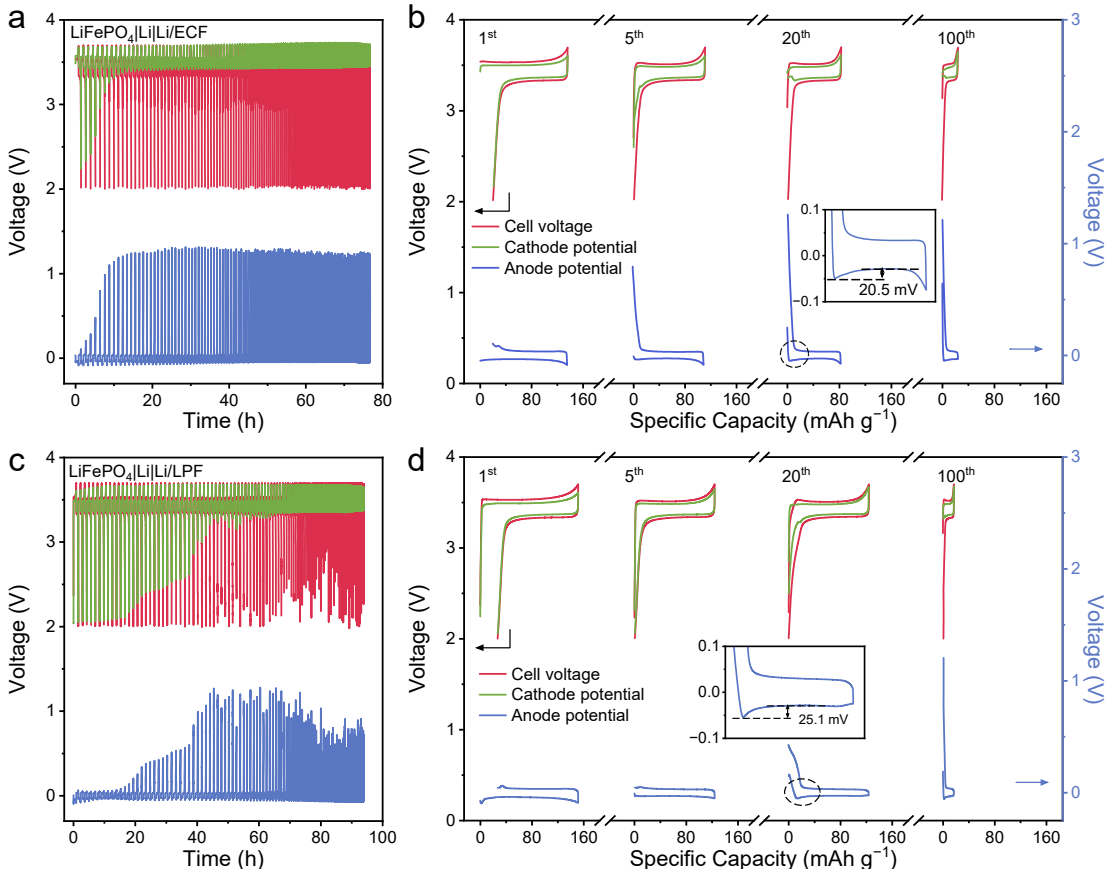

Figure S22. The voltage distribution curve of (a,b) $LiFePO_4$|Li|Li/ECF, (c,d) $LiFePO_4$|Li|Li/LPF full cell and the potential distribution of each electrode in a three electrode system, with enlarged curves for specific cycles.

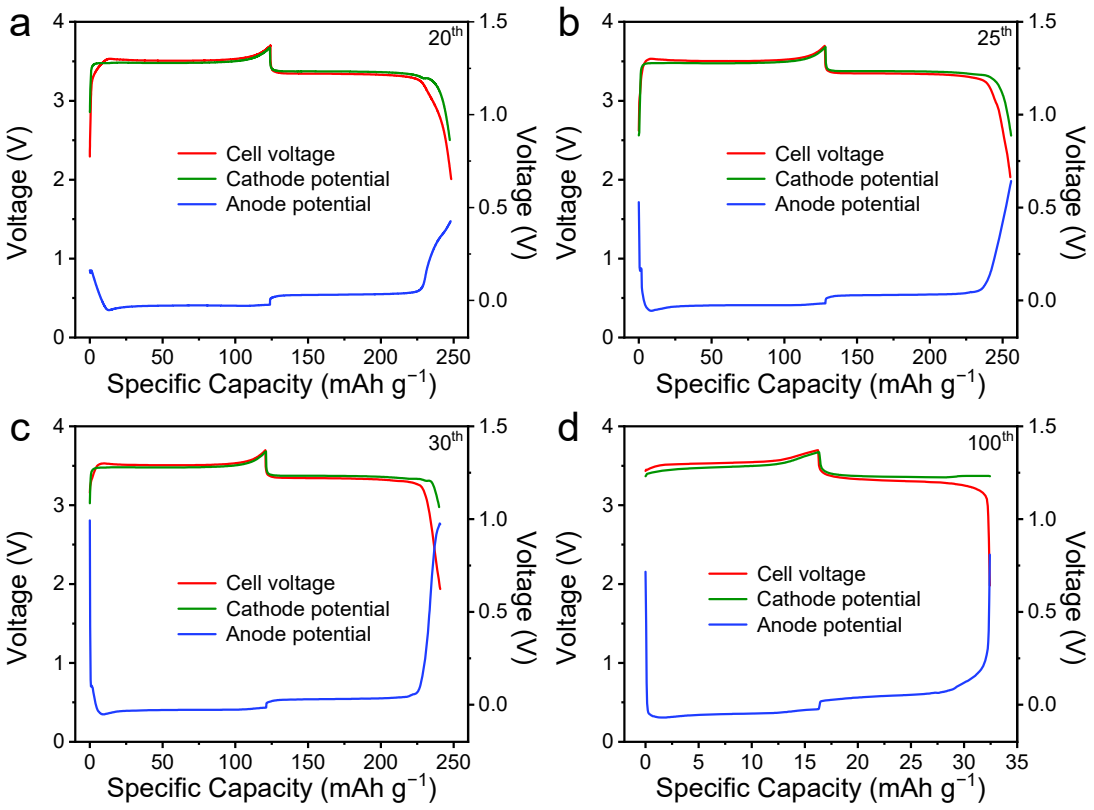

Figure S23. The potential distribution of each electrode in the $LiFePO_4$|Li|Li/LPF three electrode full cell for the (a) 20th, (b) 25th, (c) 30th, and (d) 100th cycles.

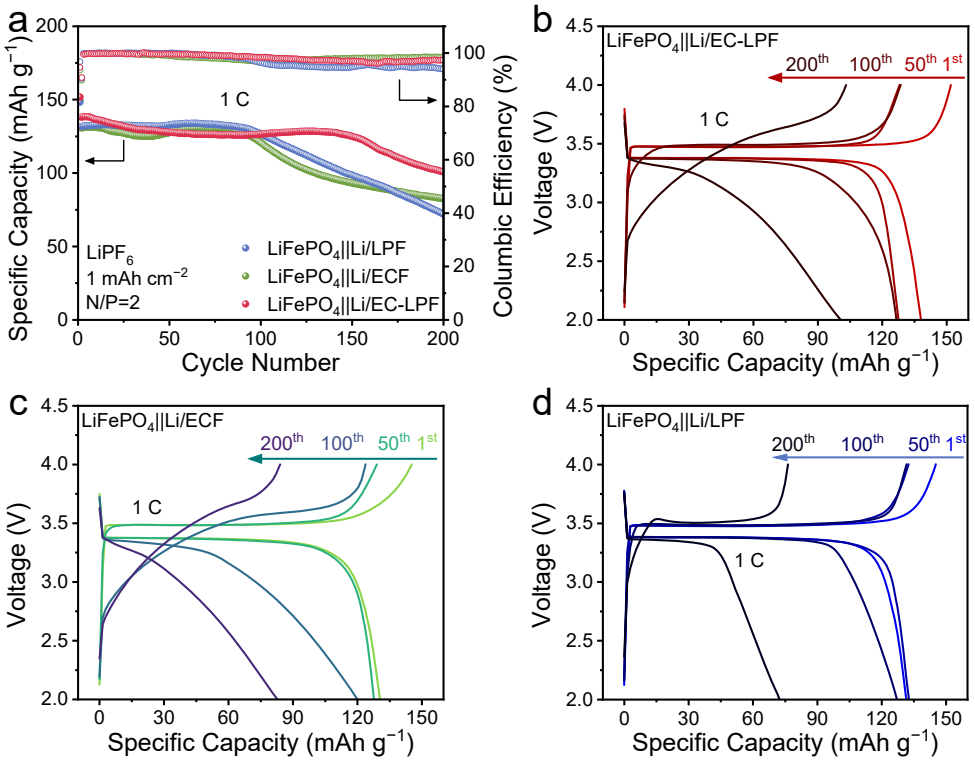

Figure S24. The cycling performance of $LiFePO_4$||Li full batteries with different self-supporting electrodes in carbonate electrolyte at 1C and (b-d) corresponding voltage profiles.

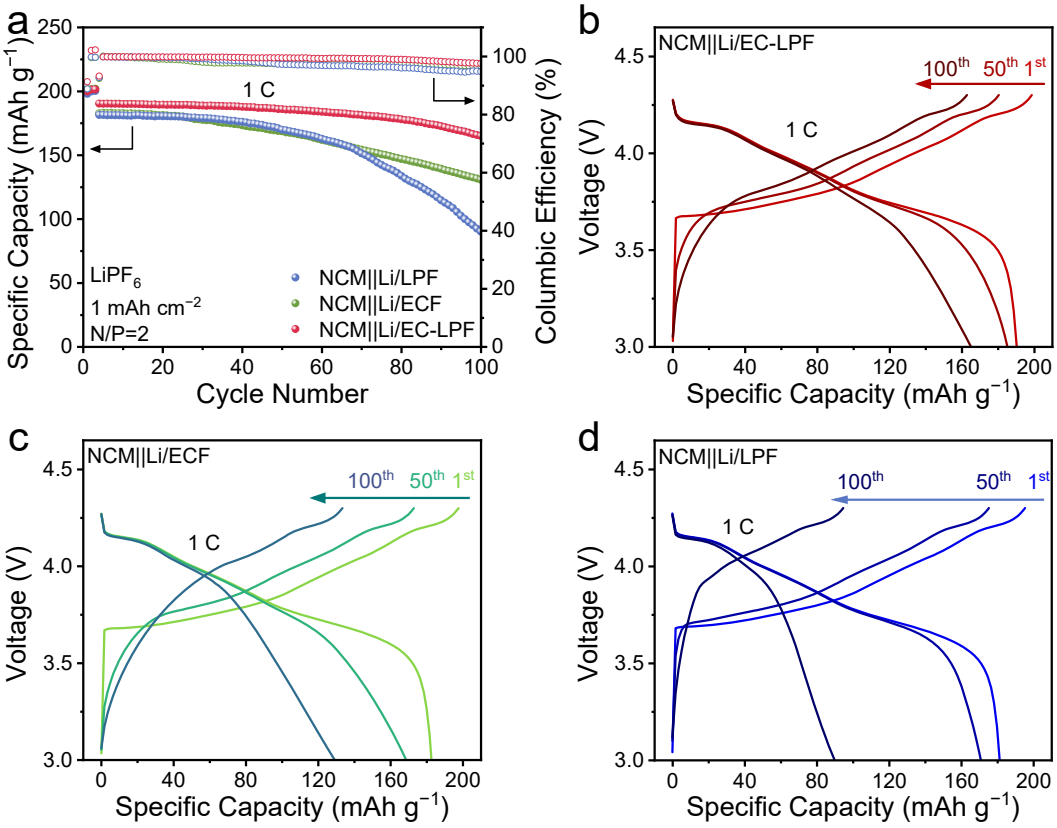

Figure S25. The cycling performance of NCM811||Li full batteries with different self-supporting anodes at 1C and (b-d) corresponding voltage profiles.

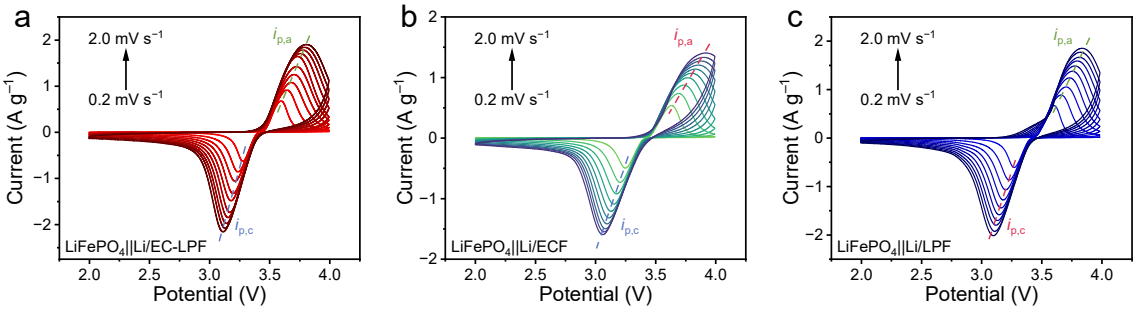

Figure S26. Typical CV curves of (a) LiFePO$_4$||Li/EC-LPF, (b) LiFePO$_4$||Li/ECF and (c) LiFePO$_4$||Li/LPF under different scan rates of 0.2, 0.4, 0.6, 0.8, 1.0, 1.2, 1.4, 1.6, 1.8, and 2.0 mV s^{-1}.

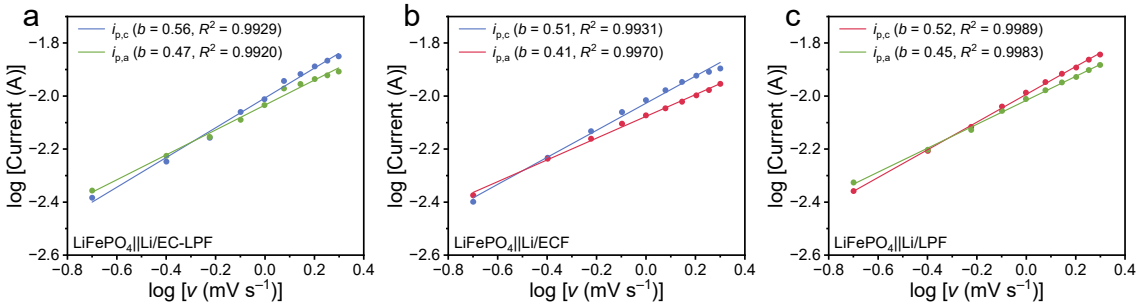

Figure S27. The relations of log(i_p) versus log(v) of (a) LiFePO$_4$||Li/EC-LPF, (b) LiFePO$_4$||Li/ECF and (c) LiFePO$_4$||Li/LPF under different scan rates.

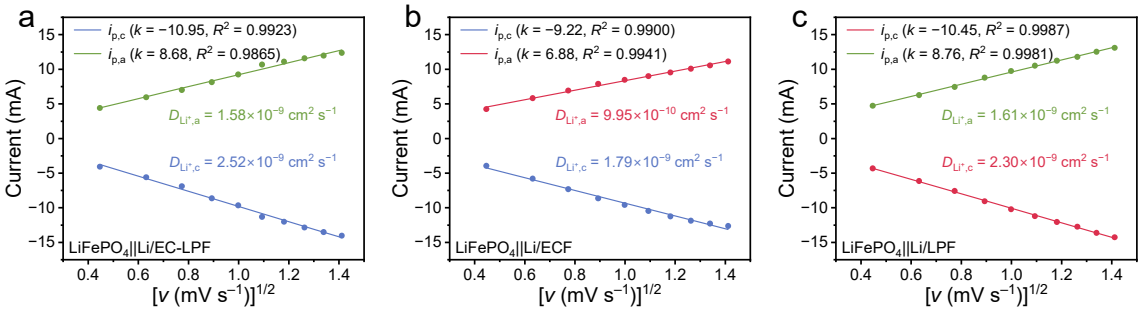

Figure S28. Linear fitting of peak currents of CV curves for (a) LiFePO$_4$||Li/EC-LPF, (b) LiFePO$_4$||Li/ECF and (c) LiFePO$_4$||Li/LPF under different scan rates.

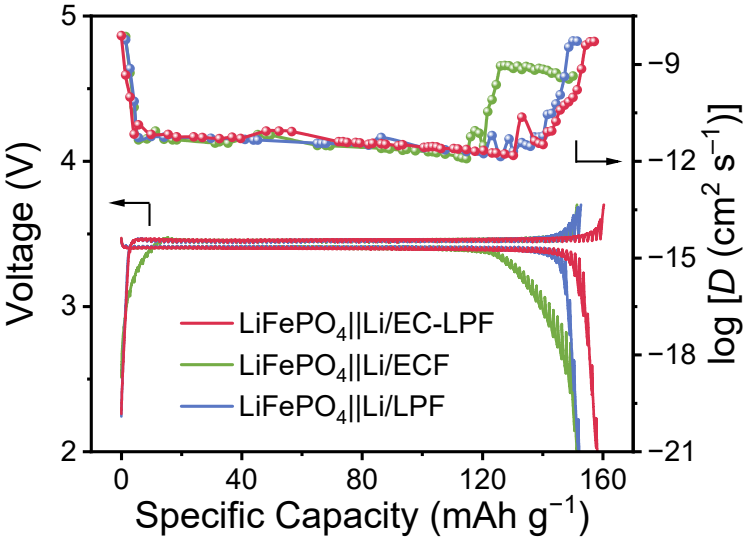

Figure S29. GITT curves and apparent Li-ion diffusion coefficients during the discharge–charge process.

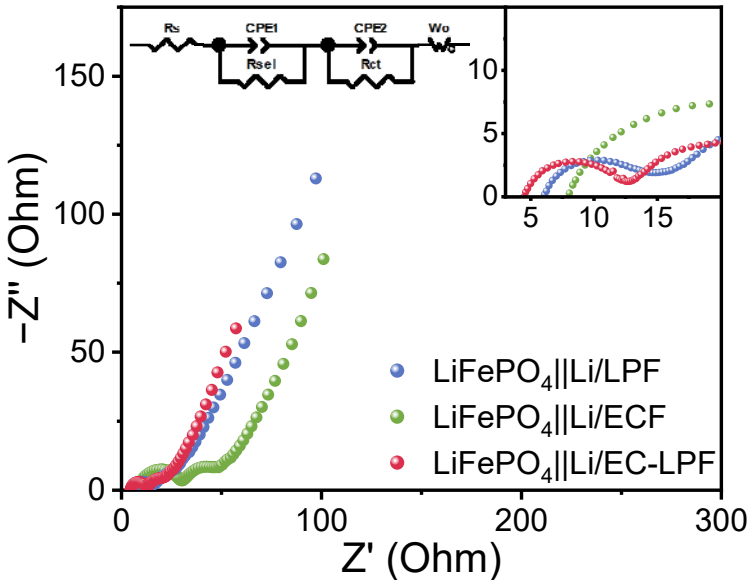

Figure S30. Nyquist plots of $LiFePO_4$||Li full cell after cycles (inset: equivalent circuit model).

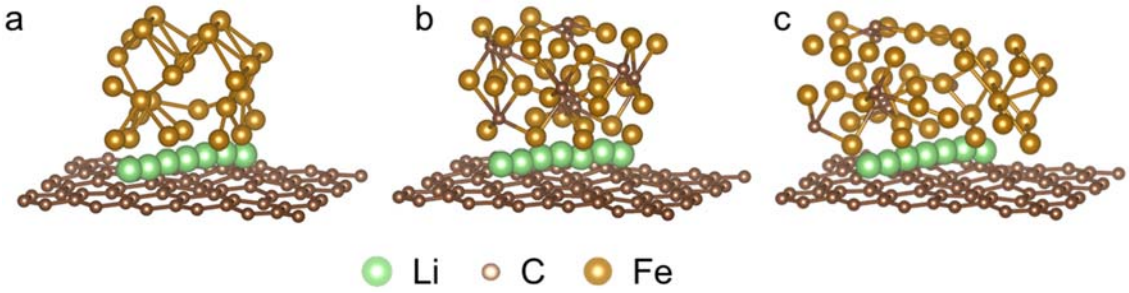

Figure S31. The migration path of Li ion in the structure of (a) Fe/C, (b) Fe_3C/C, and (c) Fe_3C/Fe/C.

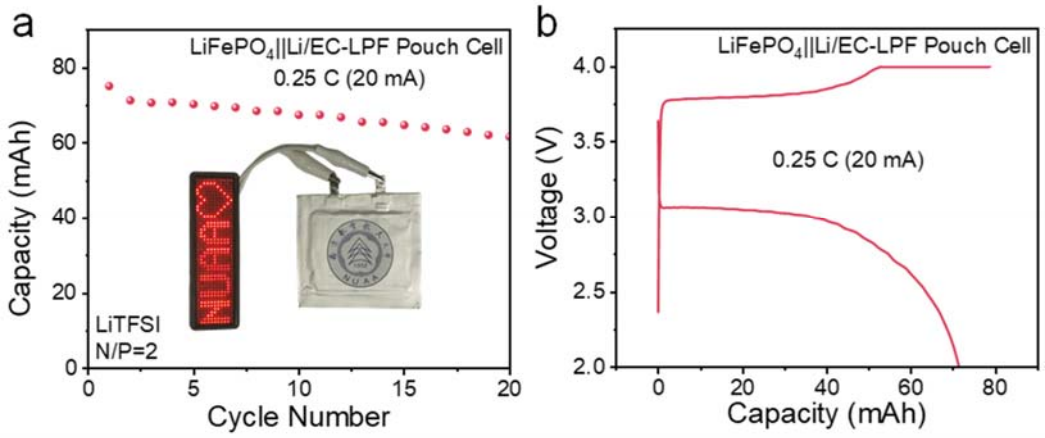

Figure S32. (a) Cycling performance of a $LiFePO_4$||Li/EC-LPF pouch cell at 0.25 C, inset: The photograph of an LED electronic badge powered by pouch cell, and (b) corresponding voltage profiles.

Table S1. Atomic percentage of solid-electrolyte interphase obtained from XPS for Li/EC-LPF, Li/ECF and Li/LPF.

Element	Atomic content (%)		
	Li/EC-LPF	Li/ECF	Li/LPF
Li 1s	21.39	32.17	28.47
C 1s	31.16	33.47	30.5
N 1s	4.05	1.24	2.07
O 1s	24.03	28.81	26.78
F 1s	12.69	2.65	8.22
S 2p	6.68	1.66	3.95

Table S2. Comparison of performance of symmetrical cells with modified metal lithium anodes reported in the past four years.

Anode	Lithium source	Li content (mAh cm^{-2})	Current density (mA cm^{-2})	Plating capacity (mAh cm^{-2})	Time (h)	REF
EC-LPF	**Electrodeposited lithium**	**3**	**1** **3**	**1** **1**	**960** **400**	**This work**
Ag@carbon macroporous fibers	Electrodeposited lithium	6	1	1	1000	Sci. Adv. 2021, 7, eabg3626
Ag-rGO-vertically aligned nanoporous block-copolymer	Electrodeposited lithium	2	1	1	400	Adv. Mater. 2022, 34, 2203992
Lotus-root-like Ni–Co hollow prisms@carbon fibers	Electrodeposited lithium	12	1	1	1200	Adv. Mater. 2021, 33, 2100608
CuO-coated PET fabric	Electrodeposited lithium	6	0.25 1	1 1	1850 450	Adv. Energy Mater. 2022, 12, 2200584
TiO_2-TiN	Electrodeposited lithium	10	1	1	200	Adv. Energy Mater. 2022, 12, 2200308
GO-PB@Cu	Electrodeposited lithium	5	1	1	300	Adv. Energy Mater. 2021, 11, 2102242
ZnO nanorod arrays/microflowers	Electrodeposited lithium	10	3	1	77	ACS Nano 2022, 16, 17454−17465
Au/Cu nanoscaffold	Electrodeposited lithium	10	1 3	1 1	1300 225	Adv. Funct. Mater. 2021, 31, 2102735
LiZn@Cu	Molten lithium	4.4	1	1	690	Nat. Commun. 2024, 15, 1354
Hydrogen-substituted graphdiyne aerogel	Molten lithium	15	1 3	1 1	600 100	Nano Lett. 2024, 24, 3044–3050
Fe-Li	Molten lithium	80 μm	0.5	0.5	700	Adv. Energy Mater. 2022, 12, 2200999
Cu_2O@Cu foam@Li	Molten lithium	85.7	3 1	1 1	150 400	Adv. Funct. Mater. 2021, 31, 2006950
S-CE/S-GE composite layer	Li foil	40 μm	5 2	3 3	400 275	Nat. Commun. 2023, 14, 4047
Li@zinc dialkyldithiophosphate	Li foil	15 μm	1	1	800	Nat. Commun. 2023, 14, 5678
Li	Li foil	5	1 3	1 1	2000 260	Nat. Energy 2021, 6, 378–387
Al-heteroatom-concentrated grain boundary	Li foil	50 μm	1	1	30	Sci. Adv. 2022, 8, eabq3445
Fluorinated carbon nanotube macro-film	Li foil	5	1	1	350	Angew. Chem. Int. Ed. 2024, 63, e202319600
F_3-Li	Li foil	600 μm	3	1	350	Angew. Chem. Int. Ed. 2023, 62, e202309622
Li_xZn_y	Li foil	64.6	1	1	900	Angew. Chem. Int. Ed. 2023, 62, e202217458
CoZn yolk-shell interlayer	Li foil	N/A	1	1	460	Angew. Chem. Int. Ed. 2023, 62, e202217476

Anode	Lithium source	Li content (mAh cm^{-2})	Current density (mA cm^{-2})	Plating capacity (mAh cm^{-2})	Time (h)	REF
ZeroVE-Li	LiMg alloy foil	13.2	1	1	1500	Adv. Mater. 2022, 34, 2205677
PDDA-TFSI@Li	Li foil	19.4	1	1	1000	Adv. Mater. 2021, 33, 2007428
FeF_3-FeF_2-LiF@Li	Li foil	N/A	1	1	1000	Adv. Energy Mater. 2022, 12, 2103332
$CuCl_2$	Li foil	N/A	4	1	200	Adv. Energy Mater. 2022, 12, 2103480
Li_2S	Li foil	300 μm	1	1	500	Adv. Funct. Mater. 2021, 31, 2006380

Note: If the original data is not provided in the literature, the lithium anode is replaced with 100 μm lithium foil.

Table S3. Fitted results of equivalent circuit for EIS data in Figure S30.

	R_s (Ω)	R_{SEI} (Ω)	R_{ct} (Ω)
EC-LPF	4.6	6.9	10.0
LPF	6.1	7.0	18.8
ECF	8.0	21.4	20.6

Table S4. Comparison of the electrochemical performance of modified metal lithium anodes paired with $LiFePO_4$ cathodes reported over the past four years in full batteries.

Anode	Area capacity (mAh cm^{-2})	N/P	Current density (mA g^{-1})	Cycle (n)	Specific capacity (mAh g^{-1})	Capacity retention (%)	Platform voltage (V)	Energy density (Wh kg^{-1})*	REF
Fe_2O_3-Fe_3C/CNF	**1.2**	**2**	**1C**	**500**	**139**	**66%**	**3.38**	**438**	**This work**
Li@eGF	3.2	1.2	0.5C	200	126	81%	3.35	400	Nat. Energy 2021, 6, 790-798
*x*PCMS-g-PEGMA/lithiated Nafion	2	46.5	0.2C	100	155	94%	N/A	170**	Nat. Nanotechnol. 2022, 17, 613-621
			0.5C	100	150	93%	N/A	165**	
LiZn@Cu	1.3	3.4	0.5C	230	140	98%	3.35	415	Nat. Commun. 2024, 15, 1354
CS/DF-PEG-DF@Li	3.4	2.9	0.5C	100	138	60%	N/A	403**	Nat. Commun. 2023, 14, 4018
Ag@carbon macroporous fibers	0.68	8.8	1C	250	132	96%	3.34	317	Sci. Adv. 2021, 7, eabg3626
Fluorinated carbon nanotube macro-film	0.85	5.9	1C	220	122	81%	3.1	300	Angew. Chem. Int. Ed. 2024, 63, e202319600
Cationic phosphonium fluoropolymers	1.73	N/A	1C	210	150	95%	3.38	350**	Angew. Chem. Int. Ed. 2023, 62, e202308724
Ordered PA-LiOH biphase layer	1.7	N/A	0.5C	200	142	98%	3.32	311**	Angew. Chem. Int. Ed. 2023, 62, e202305723
F_3-Li	1.79	22.4	1C	700	143	94%	3.31	317	Angew. Chem. Int. Ed. 2023, 62, e202309622
Li_xZn_y	0.68	95	1C	500	141	80%	N/A	90**	Angew. Chem. Int. Ed. 2023, 62, e202217458
PPy-filled HKUST-1@Cu	0.9	5.3	1C	800	150	85%	3.32	403	Angew. Chem. Int. Ed. 2022, 61, e202116291
N-doped amorphous Zn–carbon multichannel fibers decorated with carbon cages	0.8	7.8	1C	200	133	105%	3.32	328	Angew. Chem. Int. Ed. 2021, 60, 8515
C@MoS_2/S-Cu	0.5	9.8	1C	300	145	95%	3.38	342	Angew. Chem. Int. Ed. 2020, 59, 15839–15843
	1.82	3.5	1C	145	135	99%	N/A	387**	
$LiAlO_2$-Li	0.90	22.2	1C	800	142	64%	3.35	241	Adv. Mater. 2024, 36, 2303710

Anode	Area capacity (mAh cm^{-2})	N/P	Current density (mA g^{-1})	Cycle (n)	Specific capacity (mAh g^{-1})	Capacity retention (%)	Platform voltage (V)	Energy density (Wh kg^{-1})*	REF
Li-B@stainless-steel mesh	2.38	2.1	1C	400	147	98%	3.32	356	Adv. Mater. 2023, 35, 2211203
LiF/LiBO–Ag@Li	0.92	21.8	1C	650	140	94%	N/A	236**	Adv. Mater. 2023, 35, 2300350
PDDA-TFSI@Li	2.8	6.9	0.5C	200	138	98%	3.36	356	Adv. Mater. 2021, 33, 2007428
Lotus-root-like Ni–Co hollow prisms@carbon fibers	1.2	6	1C	150	106	85%	3.25	273	Adv. Mater. 2021, 33, 2100608
Fe-Li	0.51	0.03	0.5C	100	145	78%	N/A	197**	Adv. Energy Mater. 2022, 12, 2200999
SF_6 plasma-induced sulfured and fluorinated interphase/Co	0.43	44	1C	200	155	92%	N/A	174**	Adv. Funct. Mater. 2023, 33, 2214987
MXene@COF	0.9	3	1.5C	150	130	82%	3.27	375	Adv. Funct. Mater. 2021, 31, 2101194
N, O-codoped carbon nanosheet array@Cu	0.6	7	0.3C (1C=150 mA g^{-1})	430	140	71%	3.35	397	Adv. Funct. Mater. 2021, 31, 2102354
Au/Cu nanoscaffold	0.9	11.8	1C	200	126	78%	N/A	274**	Adv. Funct. Mater. 2021, 31, 2102735
M-ILE@Li	1.62	6.2	0.5C	250	161	96%	N/A	417**	ACS Nano 2022, 16, 16898-16908
hydrogen-substituted graphdiyne aerogel	3	5	0.4C	170	142	98%	3.32	399	Nano Lett. 2024, 24, 3044–3050
Poly(diallyl dimethylammonium chloride) modified bamboo fibers	2.69	3.7	1 C	200	138	95%	N/A	391**	ACS Energy Lett. 2023, 8, 486-493
LBT@Li	0.34	N/A	1C	650	120	81%	3.2	107**	Nano-Micro Lett. 2022, 14, 44

* Energy density = (Cell energy × Platform voltage)/Electrode mass (including cathode material and loaded lithium);

** Use a 3.3 V voltage platform and 100 μm lithium foil to replace missing data for calculating energy density.

Reference

[1] Kresse, G.; Furthmüller, J. Efficiency of Ab-Initio Total Energy Calculations for Metals and Semiconductors Using a Plane-Wave Basis Set. Comput. Mater. Sci. **1996**, 6, 15−50.

[2] Kresse, G.; Furthmüller, J. Efficient Iterative Schemes for Ab Initio Total-Energy Calculations Using a Plane-Wave Basis Set. Phys. Rev. B **1996**, 54, 11169−11186.

[3] Perdew, J. P.; Burke, K.; Ernzerhof, M. Generalized Gradient Approximation Made Simple. Phys. Rev. Lett. **1996**, 77, 3865−3868.

[4] Kresse, G.; Joubert, D. From Ultrasoft Pseudopotentials to the Projector Augmented-Wave Method. Phys. Rev. B **1999**, 59, 1758-1775.

[5] Blöchl, P. E. Projector Augmented-Wave Method. Phys. Rev. B **1994**, 50, 17953−17979.

[6] Grimme, S.; Antony, J.; Ehrlich, S.; Krieg, H. J. Chem. Phys. **2010**, 132, 154104.

[7] J. Du, W. Wang, M. Wan, X. Wang, G. Li, Y. Tan, C. Li, S. Tu, Y. Sun, Adv. Energy Mater. **2021**, 11, 2102259.

[8] Y. Ma, L. Wei, Y. He, X. Yuan, Y. Su, Y. Gu, X. Li, X. Zhao, Y. Qin, Q. Mu, Y. Peng, Y. Sun, Z. Deng, Angew. Chem. Int. Ed. **2022**, 61, e202116291.

[9] Y. Xu, C. Zhang, M. Zhou, Q. Fu, C. Zhao, M. Wu, Y. Lei, Nat. Commun. **2018**, 9, 1720.